Theory and experiments characterizing hypervelocity impact plasmas on biased spacecraft materials

Nicolas Lee, Sigrid Close, Ashish Goel, David Lauben, Ivan Linscott et al.

Citation: Phys. Plasmas **20**, 032901 (2013); doi: 10.1063/1.4794331

View online: http://dx.doi.org/10.1063/1.4794331

View Table of Contents: http://pop.aip.org/resource/1/PHPAEN/v20/i3

Published by the American Institute of Physics.

Theory and experiments characterizing hypervelocity impact plasmas on biased spacecraft materials

Nicolas Lee,[1] Sigrid Close,[1] Ashish Goel,[1] David Lauben,[2] Ivan Linscott,[2] Theresa Johnson,[1] David Strauss,[2] Sebastian Bugiel,[3] Anna Mocker,[3] and Ralf Srama[3]
[1]*Department of Aeronautics and Astronautics, Stanford University, Stanford, California 94305, USA*
[2]*Department of Electrical Engineering, Stanford University, Stanford, California 94305, USA*
[3]*Institut für Raumfahrtsysteme, Universität Stuttgart, Pfaffenwaldring 31, 70569 Stuttgart, Germany*

(Received 5 October 2012; accepted 13 February 2013; published online 4 March 2013)

Space weather including solar activity and background plasma sets up spacecraft conditions that can magnify the threat from hypervelocity impacts. Hypervelocity impactors include both meteoroids, traveling between 11 and 72 km/s, and orbital debris, with typical impact speeds of 10 km/s. When an impactor encounters a spacecraft, its kinetic energy is converted over a very short timescale into energy of vaporization and ionization, resulting in a small, dense plasma. This plasma can produce radio frequency (RF) emission, causing electrical anomalies within the spacecraft. In order to study this phenomenon, we conducted ground-based experiments to study hypervelocity impact plasmas using a Van de Graaff dust accelerator. Iron projectiles ranging from 10^{-16} g to 10^{-11} g were fired at speeds of up to 70 km/s into a variety of target materials under a range of surface charging conditions representative of space weather effects. Impact plasmas associated with bare metal targets as well as spacecraft materials were studied. Plasma expansion models were developed to determine the composition and temperature of the impact plasma, shedding light on the plasma dynamics that can lead to spacecraft electrical anomalies. The dependence of these plasma properties on target material, impact speed, and surface charge was analyzed. Our work includes three major results. First, the initial temperature of the impact plasma is at least an order of magnitude lower than previously reported, providing conditions more favorable for sustained RF emission. Second, the composition of impact plasmas from glass targets, unlike that of impact plasmas from tungsten, has low dependence on impact speed, indicating a charge production mechanism that is significant down to orbital debris speeds. Finally, negative ion formation has a strong dependence on target material. These new results can inform the design and operation of spacecraft in order to mitigate future impact-related space weather anomalies and failures. © *2013 American Institute of Physics*. [http://dx.doi.org/10.1063/1.4794331]

I. INTRODUCTION

Space weather describes the coupled behavior of space plasmas, electromagnetic fields, and energetic particles between the Earth and the Sun. It includes effects, such as solar activity and plasma interactions, that can subject spacecraft to conditions near their design limits. Impacts of meteoroid or debris (hypervelocity impactors) on spacecraft under these conditions can cause electrical damage in addition to the better-known risk of mechanical damage. In particular, small, fast impactors ($<1\ \mu$g) are common and pose a risk of electrical damage through electromagnetic radiation, despite being too small to puncture a spacecraft surface. To assess the risk of electrical damage from hypervelocity impact, we conducted experiments leading to detection of impact-related radio frequency (RF) emission. Here we present the first characterization of the plasma produced by these impacts, including plasma composition and temperature, to link the plasma expansion dynamics to RF emission.

This work is a first step toward developing spacecraft requirements for shielding from impact-related electrical damage. This currently does not exist even for the International Space Station (ISS), which is protected against mechanical damage from up to 1-cm aluminum spheres impacting at debris speeds. Specifications for military and ISS systems (MIL-STD-461 E and SSP 30237) stipulate that systems be immune to radiated electric fields of up to 20 and 250 V/m, respectively. Specifications for immunity to *transient* radiated fields (which is what an impact would produce) are not applied to military spacecraft systems although the ISS imposes limits on susceptibility to transient magnetic fields.

Without adequate shielding, the consequence of electrical damage from hypervelocity impact can be severe, as illustrated by satellite anomalies correlated to meteoroid activity. The Olympus spacecraft lost attitude control due to a gyro anomaly during the 1993 Perseid meteoroid shower.[1] Although control was restored, the anomaly terminated the mission. The ADEOS 2 and ALOS satellites experienced power system failures during the 2003 Orionids and the 2011 Lyrids, respectively, and both spacecraft were lost. In 2009, a gyro anomaly occurred on the Landsat 5 spacecraft, again during the Perseids. Unfortunately, our limited ability to diagnose failures in space precludes unambiguous identification of impacts as the root cause.

When a hypervelocity impactor hits a spacecraft, it forms a dense plasma. Previous work has led to empirical relations for impact charge production Q. These typically take the form $Q \propto m^{\alpha} v^{\beta}$ where m is the impactor mass and v

is the impact speed. McBride and McDonnell[2] reported values of $\alpha = 1.02$ and $\beta = 3.48$, though others[3,4] have spanned the range $2.8 < \beta < 4.8$. Foschini[5] showed that the charge produced by meteoroid impacts could theoretically generate RF emission exceeding the noise level of spacecraft systems.

Through ground-based testing, researchers have measured RF emission from hypervelocity impacts on rocks[6] and optical emission from impacts on metallic targets.[7] However, little research has focused on RF emission from hypervelocity impacts as a mechanism of electrical damage to spacecraft systems. Starks *et al.*[8] reported inconclusive results from their experiments seeking RF emission although microwave emission attributed to microcracking of the target material has been measured by Maki *et al.*[9] These experiments used light gas gun and rail gun facilities with projectile masses of ~1 g, impact speeds of 1–12 km/s, and chamber pressures of ~0.1 mbar, which is not representative of hypervelocity impacts in the vacuum of space. No previous study has detected RF emission through impact plasma effects, which is the focus of this work.

Section II discusses the space weather conditions and the impactors that can affect a spacecraft and a theoretical model for RF emission. Our hypervelocity impact experiment is described in Sec. III. Section IV introduces two theoretical models that are used to describe the expanding plasma, and Sec. V discusses the plasma composition and temperature from our experimental measurements. Finally, Sec. VI suggests how this research can inform design and operation of spacecraft to mitigate this threat.

II. BACKGROUND

A principal effect of space weather on spacecraft is surface charging, caused by plasma bombardment and photoemission. The interaction of the spacecraft with the plasma environment can result in a sheath around the spacecraft as well as a trailing wake, where the plasma is perturbed from ambient conditions.[10–12] The resulting electromagnetic fields, which can be time-varying and non-uniform, as well as expansion into an ambient plasma, can modify the motion of an impact plasma or result in instabilities.

Meteoroids are naturally occurring solid bodies in the solar system, defined as smaller than asteroids (<1–10 m) and larger than atoms. Most meteoroids travel at speeds between 11 and 72.8 km/s. However, meteoroids smaller than ~1 μm, for which photon pressure and electrodynamic forces exceed gravity,[13] as well as interstellar meteoroids that originate outside the solar system,[14] could produce greater impact speeds. The number flux of meteoroids is roughly inversely proportional to the mass of the meteoroid squared.[15] This dependence is more commonly reported as a cumulative number flux where the total number of meteoroids with mass greater than a given mass m is proportional to m^{-1}. For example, Close *et al.*[16] report an exponent of -0.94 ± 0.2, while Brown *et al.*[17] report an exponent of -0.90 ± 0.03. The distribution of small meteoroids and in particular the interstellar population is not well characterized, in part due to instrument biases.[18]

Orbital debris includes all the non-functioning objects derived from human activity in space. The population is predominantly in low Earth orbit (LEO) and includes objects ranging from small paint chips up to discarded rocket bodies. The average impact speed in LEO is approximately 10 km/s.[19]

Hypervelocity impact plasmas are composed of material from the impactor and the impact surface, and are formed through partial conversion of kinetic energy into vaporization and ionization energy.[20,21] The initial plasma is highly collisional and quickly equilibrates. As it expands, the collision rate falls, allowing free electron oscillation at the plasma frequency.[22] This can result in RF emission. The collision rate, expansion speed, and consequently the emission spectrum are determined primarily by the composition and temperature of the plasma. As the plasma rarifies, external fields can separate the plasma species by their mass and charge, producing further RF emission through a current pulse.

III. HYPERVELOCITY IMPACT EXPERIMENTS

We studied the plasma expansion and associated RF emission from impacts under a range of surface charging conditions, through experiments conducted in 2011 using a Van de Graaff dust accelerator at the Max Planck Institute for Nuclear Physics.

The accelerator is described in detail by Mocker *et al.*[23] Positively charged dust particles are accelerated through electrostatic repulsion from a 2 MV terminal. Each particle's speed is limited by its maximum surface charge, based on the conversion of electrical potential energy into kinetic energy. In this experiment, iron particles were used; Figure 1 shows the particle distribution and the corresponding theoretical charge production. The particles impact a target inside a 1.4 m test chamber. Our tests were conducted at pressures between 3.0×10^{-6} and 1.0×10^{-5} mbar, corresponding to a mean free path longer than the chamber diameter and allowing for free expansion of the impact plasma, similar to conditions on orbit.

A. Impact targets

The targets (Figure 2) were selected to study impacts on spacecraft materials as well as bare metals. To provide a geometry representative of spacecraft, most of the targets were

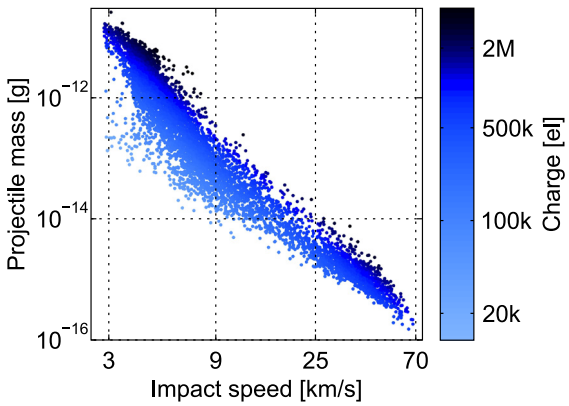

FIG. 1. Projectile distribution, color-coded for theoretical charge production using the relation $Q \sim m^{1.02} v^{3.48}$. Note the strong dependence of speed and mass.

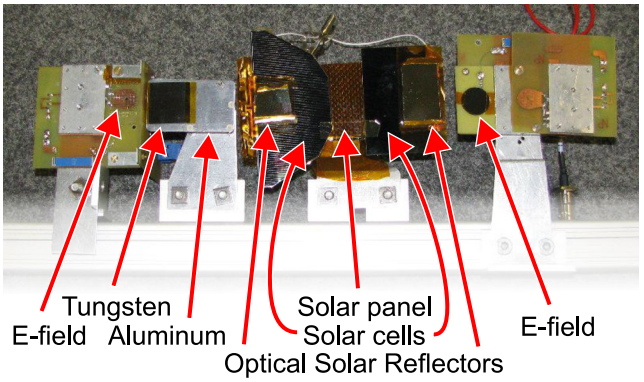

FIG. 2. Impact targets used in the experiment.

used without any accelerating or focusing grids. Surface charging through space weather was simulated by biasing the targets using a high-voltage supply. Tungsten and aluminum samples were used as baseline targets and were biased through a current-limited connection to the high-voltage supply. Samples of representative spacecraft materials were donated by Lockheed Martin, including solar panel substrate, two solar cells (one with uncoated cover glass in a LEO configuration, and the other with a conductive coating in a GEO configuration), and two optical solar reflectors (OSRs), with and without a conductive coating. The aluminum honeycomb within the solar panel substrate and the interconnects on the solar cells were connected to the high-voltage supply. The OSRs were placed on top of the solar cells but were not directly connected to a bias voltage. Several configurations of an active target were used, with an electric field (E-field) antenna as the target surface. One of these electric field sensors was the only target to use an accelerating grid. In this paper we limit our discussion to impacts on tungsten and on the spacecraft materials in order to understand how plasma parameters vary with target material and bias, and impact speed.

B. Sensor suite

Impact events were observed by optical, RF, and plasma sensors, arranged around the 30° inclined target (Figure 3). A photomultiplier tube detected optical emission and provided impact timing. Six patch antennas tuned to 315 MHz and 916 MHz were arrayed to record RF emission. These frequencies span a range from a wavelength close to the chamber dimensions up to the bandwidth limit of the oscilloscopes used. Two electric field sensors served as targets while another two observed radiated electric fields. Three different plasma sensors were designed and built at Stanford University to measure the net current produced by the expanding plasma. The RF detection by the patch antennas was limited to fast impacts on highly biased tungsten targets. Here we focus on plasma measurements to compare these impact conditions with other materials, target biases, and speeds.

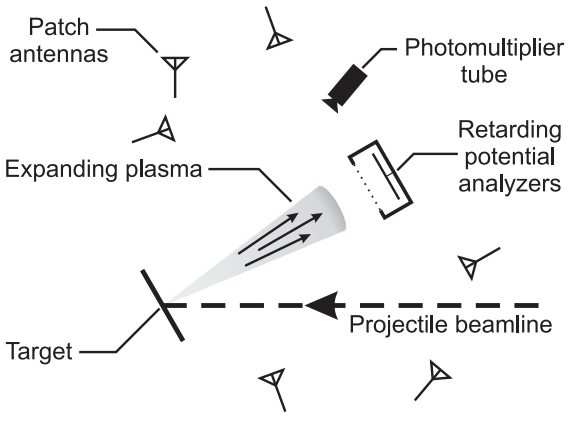

FIG. 3. Sensor configuration within the test chamber.

Of the three plasma sensor arrangements, a set of two retarding potential analyzers (RPAs) was first placed in front of the impact point at distances of 65 and 85 mm and at an angle of 30° in azimuth from the target surface normal vector. The RPA design is conventional and similar to that described by Heelis and Hanson.[24] However, most impacts (including all results discussed in this paper) were recorded with all grids set at chamber ground potential to measure the net current deposited on the collector. The collector plate is a plated pad on a printed circuit board. It is connected to a transimpedance amplifier that converts the deposited current into a voltage signal. The amplifier's frequency response is well represented by a third-order linear time-invariant system with maximum gain between 10 Hz and 1 MHz. This was validated through simulation and calibration using an electron gun.

The RPA pair was then replaced with a set of four charge-sensitive plates arrayed at constant distance but varying angle and finally a set of four plates arrayed at constant angle but varying distance from the impact point. These were identified as Faraday plate arrays (FPAs) spanning theta (angle) and range. These were designed and built to make measurements of the impact plasma with different collector geometries. The sensors use the same amplifiers as the RPAs, while each collector plate is a circular copper sheet and is shielded behind by a grounded copper cup. FPA-theta has four collectors positioned at ± 23° and ± 68° in azimuth, and FPA-range has collectors positioned 30, 50, 60, and 90 mm from the point of impact, which are sized to span approximately constant solid angle. The three plasma sensors are shown in Figure 4.

C. Experimental results

During the experimental campaign, over 6000 impact events were recorded, spanning target materials, bias configurations up to ± 1kV, impact speeds from 2–60 km/s, and projectile masses from 0.1 fg to 10 pg (10^{-16} to 10^{-11} g). A summary of the 3348 impacts on the targets discussed in this paper is presented in Table I. The bare tungsten target was selected for a focused study of the effect of target bias. The spacecraft materials were uniformly tested at a representative negative bias of −300 V. Two of the spacecraft materials (the LEO solar cell and the standard OSR) were selected for analysis of positive ion composition using a bias of +100 V. The LEO solar cell was also studied under a range of lower negative biases. Figure 5 shows unprocessed plasma, optical, and RF measurements from one event with detected RF emission. The signal amplitudes are plotted as the measured

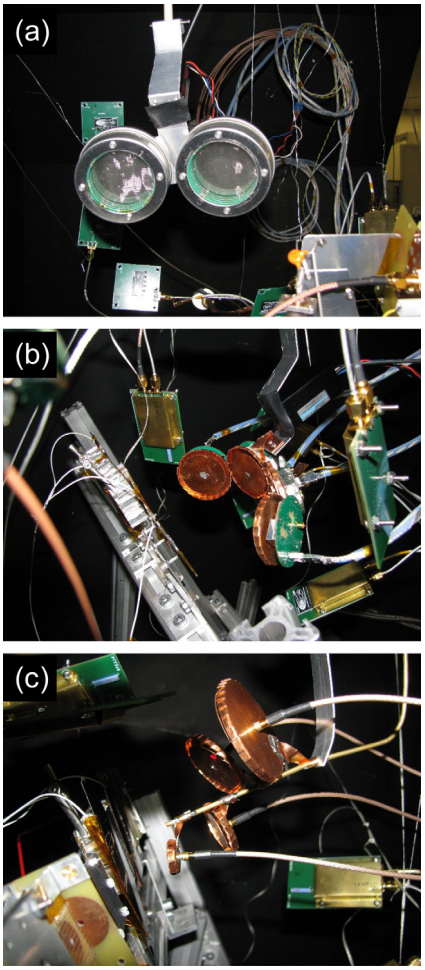

FIG. 4. Photos of the plasma sensors in the chamber, from top to bottom: (a) RPAs, (b) FPA-theta, and (c) FPA-range.

voltage at the oscilloscopes. This was a 3.9 fg projectile hitting a −1 kV biased tungsten target at 35.3 km/s. The RPAs detect an electron pulse correlated in time with the RF emission detected at 315 MHz. To understand the characteristics of the impact plasma during the time that it is producing this RF emission, we connect the relevant plasma parameters to the measurements made by the RPAs using physics-based models.

IV. PLASMA EXPANSION MODELS

Hypervelocity impacts produce plasmas that are initially extremely dense ($\sim 10^{23}$ m^{-3}) but small ($\sim 1\,\mu$m), limiting our ability to directly measure the plasma until it has expanded and rarified. In this section, one model is presented to link experimental measurements to plasma composition and final temperature, and then a second model to establish the plasma temperature earlier in the expansion process.

As the plasma is formed and reaches thermal equilibrium, its motion can be described by the plasma momentum equation for each species

$$mn\left[\frac{\partial \vec{v}}{\partial t} + (\vec{v}\cdot\vec{\nabla})\vec{v}\right] = qn(\vec{E} + \vec{v}\times\vec{B}) + mn\vec{g} - \vec{\nabla}\cdot\overleftrightarrow{P} + mn\nu\vec{v}. \quad (1)$$

TABLE I. Summary of impact measurements on the materials discussed in this paper.

		Targets						
		W	SP	SC-GEO	SC-LEO	OSR-Std	OSR-Con	Total
Target bias	−1000 V	336						336
	−850 V	87						87
	−750 V	115						115
	−500 V	170						170
	−300 V	154	148	72	148	43	202	767
	−100 V	3			155			158
	−75 V				17			17
	−50 V	124			11			135
	−40 V				18			18
	−30 V				77			77
	GND	304			49		49	402
	+0 V[a]	20						20
	+5 V	41						41
	+10 V	83						83
	+20 V	85						85
	+30 V	30						30
	+40 V	46						46
	+50 V	137						137
	+100 V	60			64	102		226
	+300 V	111						111
	+500 V	38						38
	+1000 V	219						219
	FLOAT	30						30
	Total	2193	148	72	539	145	251	3348

[a]+0 V refers to a configuration where the target is connected to the bias supply voltage and is driven to zero, rather than directly shorting the bias line to the chamber wall.

Here, m, n, q, and $\vec{v}$ are the mass, number density, charge, and velocity of the plasma. $\vec{E}$ and $\vec{B}$ are the electric and magnetic fields, $\vec{g}$ is the gravitational acceleration, $\overleftrightarrow{P}$ is the pressure tensor, and ν is the collision rate between plasma particles. The four force terms on the right side of the equation can vary significantly through the impact plasma expansion process.

The external magnetic field and gravitational terms are small enough to be neglected over the time and length scales of interest. For an impact plasma under the influence of the geomagnetic field, the electron Larmor radius is on the order of 1 m at the Earth's surface and even larger in space. While the plasma density is high, the collisional and pressure terms dominate. Because the plasma quickly equilibrates, its velocity distribution will be isothermal, isotropic, and Maxwellian, so

$$\vec{\nabla}\cdot\overleftrightarrow{P} = \nabla(nk_BT) = k_BT\nabla n, \quad (2)$$

where k_B is the Boltzmann constant and T is the temperature. The plasma is shielded from external electric fields and expands at its thermal speed, which for each species j is

$$v_{th,j} = \sqrt{\frac{k_BT_j}{m_j}}. \quad (3)$$

Here m_j is the mass of the particles of species j. The plasma frequency

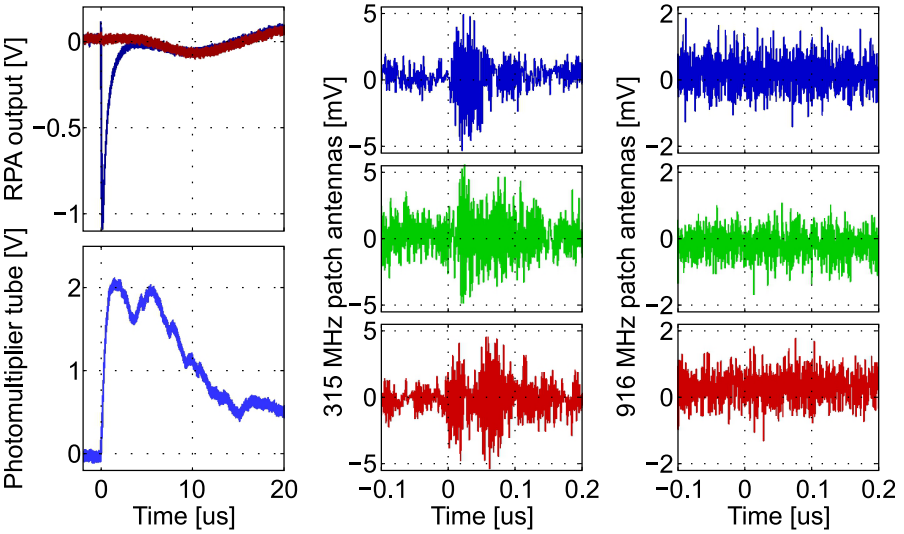

FIG. 5. Simultaneous measurements from a single impact of a 3.9 fg projectile on −1 kV tungsten at 35.3 km/s.

$$\omega_{p,e} = \sqrt{\frac{n_e e^2}{\epsilon_0 m_e}} \tag{4}$$

is the oscillation frequency of electrons around the ion population. In addition to RF energy produced by the oscillation, the motion can couple with instabilities that amplify the emission. RF emission linked to electron oscillations will drop in frequency with plasma density, resulting in an electromagnetic pulse with a falling chirp signal.

With further expansion, the Debye length eventually exceeds the plasma radius, allowing an external electric field to penetrate. At this point, the charge population violates certain definitions of plasmas since it has large electric potentials. However, for clarity we will continue to refer to the population as an impact plasma. With a strong enough external field, the positive and negative species separate, resulting in a current pulse which can also produce RF emission.

Measuring the fractional composition of the plasma provides the mass distribution of the particles, and the temperature of each species provides the velocity distribution. These parameters strongly influence the thermal and ion acoustic speeds associated with the expanding plasma. The plasma temperature also affects the Coulomb collision rate, which determines the density at which free electron oscillations can occur.

Composition of the plasma will not change much through the expansion; there is no significant mechanism for additional ionization or recombination once the plasma becomes non-collisional. However, the plasma temperature is more complicated. In the early, dense plasma, the concept of temperature is conventional; within any small volume is a distribution of velocities. However, as the plasma rarifies, the fastest particles will travel farther, spatially filtering the velocity distribution. Nevertheless, by accounting for the entire population, the velocity distribution remains well defined.

A. Single particle motion

For much of the plasma expansion, the only significant force acting on the plasma particles is from the external electric field. The particles are too distant to impose substantial electrostatic forces on each other, and other external forces are much weaker. This stage is referred to as *single particle motion* (SPM) because each particle moves individually, and describes the plasma motion within the range of 1–10 cm. By assuming 1D motion under the influence of a uniform external electric field E_{ext}, the equation of motion for a charged particle can be written as $F = m\ddot{x} = qE_{ext}$. This equation is integrable, allowing a particle's initial speed to be expressed as

$$v_0(t) = \frac{d}{t} - \frac{qE_{ext}t}{2m} \tag{5}$$

if it travels a distance d in some time t. This relationship is shown in Figure 6, where particle trajectories are plotted in space time for three ion species, producing current pulses at

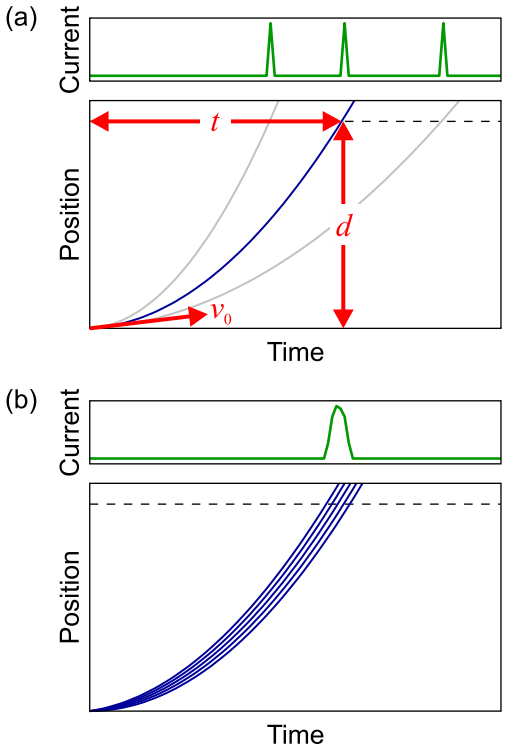

FIG. 6. (a) Parameters in the SPM model. (b) Initial speed distribution causes the measured current peak to spread out.

the indicated position. Here we assume a positively charged target with an electric field oriented away from the impact surface that accelerates positive ions outward. If the target were negatively charged, the electric field would be reversed such that electrons and negative ions would be accelerated from the impact surface. With an initial speed distribution, the times-of-flight for a single ion population will spread, causing a wider current pulse. The pulse width is therefore a measure of the speed distribution and the plasma temperature.

The velocity distribution at the onset of SPM can be derived from temperature by assuming a Maxwellian or half-Maxwellian distribution using the density function

$$f_q(v) = \eta_j Q \sqrt{\frac{2m_j}{\pi k_B T_j}} \exp\left(-\frac{m_j v^2}{2k_B T_j}\right), \tag{6}$$

where Q is the total charge and η_j is the fraction of species j. Using a positive half-Maxwellian distribution discounts the particles with negative initial velocity, which would hit the target and not reach the plasma sensor. The plasma current is

$$I(t) \approx \sum_j \frac{\eta_j Q}{\delta t}\left[\operatorname{erf}\left(\sqrt{\frac{m_j}{2k_B T_j}} v_0(t)\right) - \operatorname{erf}\left(\sqrt{\frac{m_j}{2k_B T_j}} v_0(t+\delta t)\right)\right], \tag{7}$$

computed by integrating over a band of initial velocities. With the amplifier response, this model produces a synthetic measurement based on a plasma composition and temperature, which can be compared against measurement.

B. 1D conical numerical simulation

Looking earlier in time from the SPM state, the next relevant force acting on the plasma is from the internal electrostatic fields imposed by the charged particles on each other. Accounting for this force allows the plasma motion to be described starting from millimeter sizes rather than centimeter. The equation of motion can be augmented to become $F = m\ddot{x} = q(E_{int} + E_{ext})$ but must be integrated numerically.

To perform this integration, the plasma is discretized into shells of spherical caps constrained to move in 1D over a fixed cone angle, selected to be 15°, based on the geometry of the two RPAs and the observed difference in the measurements from each. Each shell is composed of a single species with a single velocity; multiple shells are used to discretize each species' velocity distribution. The shells are infinitesimally thin with uniform charge. The cone vertex depth x_d is computed such that the cone is tangent to a sphere of the initial plasma radius (Figure 7). The initial positions of the shells are selected to populate the keystone-shaped segment containing the initial sphere. Each shell has an associated electric field that is imposed on all other shells. This electric field is depicted in Figure 7(b). To conserve linear momentum, the position of each shell is tracked by the location of the point where its associated electric field is zero.

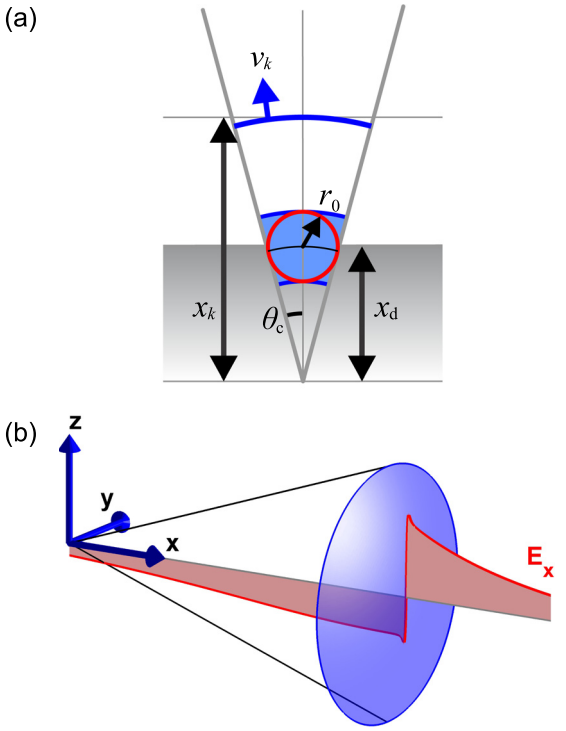

FIG. 7. (a) Geometry of plasma expansion cone and initial shape of discretized plasma shells. (b) Spherical cap geometry and internal electric field.

V. RESULTS

The data collected from the ground-based experiments described in Sec. III are combined with the models presented in Sec. IV to provide an understanding of the relevant plasma parameters (composition and temperature) governing the motion of impact plasmas for a range of conditions. The SPM model is computationally fast, so it is used to iterate over plasma parameters while fitting to experimental data. The numerical simulation is better suited to the study of individual configurations.

A. Impact plasma composition

The ion composition of the impact plasma has a significant role in its expansion dynamics and RF emission. Lighter ions will expand more quickly, resulting in a stronger current pulse but less time for electron oscillation. To determine composition, measured current peaks are matched with corresponding ions using the SPM model. Doubly ionized particles were considered but none corresponded to expected species. The following analysis assumes all particles are singly ionized.

1. Baseline tungsten impact

The impact of a 3.4 fg projectile on +1000 V tungsten at 35.2 km/s provides a measurement of positive ion composition in a configuration with large charge production. Figure 8 shows the measurement with the model output. The fractional composition is 25% H, 12% C, 9% O, 3% Na, 31% Fe, and 20% W with temperatures of ~20 eV for the bulk species.

Using this baseline impact plasma population, the plasma density was computed over space and time to

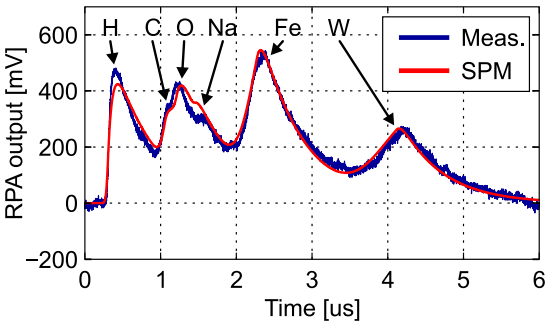

FIG. 8. Measurement of six ion species from a 3.4 fg projectile traveling 35.2 km/s impacting tungsten biased at +1000 V, with SPM output.

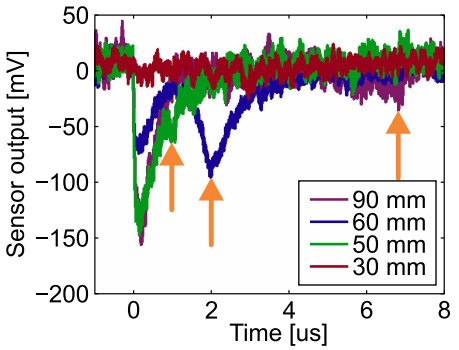

FIG. 10. A 4.55 km/s impact of a 5.6 pg projectile on −300 V tungsten. The negative ion signal is indicated by the orange arrows.

determine Debye length and pressure gradient. For length scales greater than 1 mm, the Debye length exceeds the plasma radius, and the pressure gradient force does not exceed the external electrostatic force. These thresholds indicate that the assumptions made for both expansion models are valid.

2. Impacts on tungsten vs. target bias

Representative waveforms from positively and negatively biased and grounded tungsten are shown in Figure 9. With the highly biased targets, the electric field focuses the expanding plasma toward the RPAs. A bifurcation in the electric field is created by the gap between the sensors. The asymmetry in the RPA positions relative to the impact point focuses the expanding plasma consistently into the nearer RPA.

The measurements from fast impacts on the tungsten target with low bias (between 0 and +50 V) show a peak corresponding to H. However, the predicted W and Fe populations are not detected. If they are present, they may be masked by an electron population, supporting the possibility of RF emission through electron oscillation. Similar measurements are observed up to target bias voltages of +50 V, but not below impact speeds of 30 km/s.

With high negative target bias, electrons hit the RPA with enough energy to cause secondary electron emission (SEE). For tin which is the predominant metal in the RPA collector, the SEE yield from electron bombardment is greater than unity above primary energies of ∼200 eV.[25] This causes a signal with a bipolar response. Because of their high mobility, the electrons produce a much stronger current pulse than ions; this is likely the cause of the detected RF in the patch antennas. In some impacts on negatively biased targets, negative ions are detected. A measurement using the range-varying collector plates is shown in Figure 10; the timing difference for the second pulse at each range indicates that ions are the cause and not a subsequent emission of electrons. The presence of negative ions suggests a reduction in the free electron population and therefore reduced RF emission.

3. Impacts on spacecraft materials

All five spacecraft materials were tested while biased at −300 V. The measurements from these negatively-biased targets show significant variation depending on target material (Figure 11). The solar panel and conductive solar cell show only a small negative ion population (likely Fe), while the uncoated solar cell and conductive OSR show the negative ion signal more strongly. The standard OSR shows an additional heavier negative ion species which has not yet been identified.

4. Impacts on tungsten vs. impact speed

The SPM model was used with twelve other impacts on +1000 V tungsten to compute the fractional compositions as a function of impact speed (Figure 12). The Fe and W content in the plasma remain high over the range of impact speeds. The faster impacts contain H, C, and O, while the slower impacts contain Na and K. The presence of increased contaminant species at slower impact speeds is well-documented.[4] These alkali metals with low ionization energies are attributed to surface contamination. The contaminant species at higher impact speeds are likely dissociated hydrocarbons which may be due to human contact with the target.

5. Impacts on spacecraft materials vs. impact speed

Only the uncoated solar cell and the conductive OSR were tested at a positive bias (+100 V). The cumulative

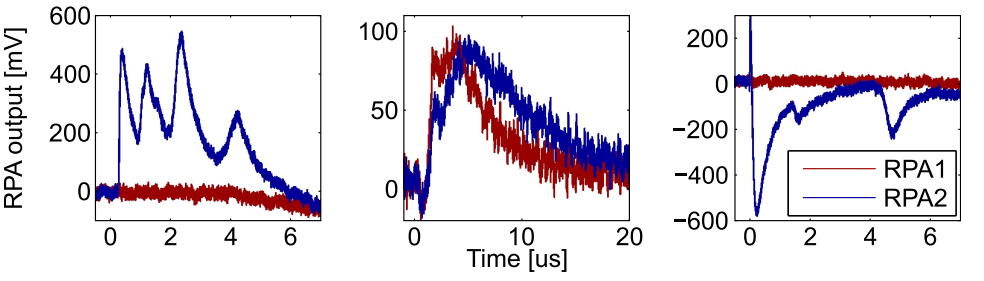

FIG. 9. Impacts on tungsten target. The red trace is from the RPA placed 85 mm from the impact point, and the blue trace is from the RPA placed 65 mm from the impact point. Left to right: same impact as in Figure 8; 0 V target with a 2.3 fg projectile impacting at 45.3 km/s; −1000 V target with a 27 fg projectile impacting at 3.5 km/s.

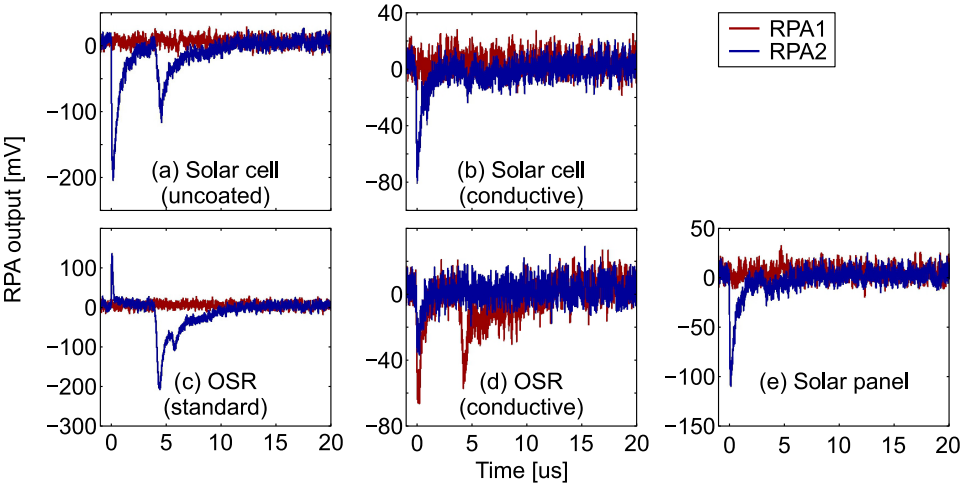

FIG. 11. Impacts on the −300 V spacecraft targets. The presence of negative ions is highly dependent on target material. The projectile masses are: (a) 0.59, (b) 6.9, (c) 13, (d) 7.6, and (e) 6.7 fg, respectively. The impact speeds are (a) 59.2, (b) 18.7, (c) 21.6, (d) 18.3, and (e) 19.4 km/s, respectively.

measurements are shown in Figure 13 along with +1000 V tungsten. Impacts on the solar cell show little dependence of composition on impact speed. Unlike the species present from tungsten impacts, the two species apparent from solar cell impacts (Si and Fe) remain at roughly constant proportion from impact speeds of over 60 km/s down to 10 km/s, indicative of a different ionization mechanism. This trend is less apparent for OSR impacts, which show a hydrogen peak for fast impacts and a more noticeable drop in the amplitude of the iron peak for slower impacts.

B. Initial plasma temperature

The plasma population computed in Sec. V A 1 for the baseline tungsten impact was simulated using the 1D conical model with 100 shells and a 2 mm initial radius. Because this population was determined using the SPM model, it neglects the effect of internal electrostatic forces. When accounting for these forces, the initial temperature (∼20 eV) results in too much dispersion in time. An order of magnitude reduction in the initial temperature restores the fit to the measurement (Figure 14). The inclusion of internal electrostatic forces has the effect of repelling like charges from each other during the initial expansion. This results in a velocity distribution that is wider than it was initially. The implication is that the temperature as measured after the plasma has expanded represents a velocity distribution after the particles have pushed themselves apart, and the initial distribution is narrower with a correspondingly lower temperature. Previous studies of impact plasma energetics[4] reported measurements of 10–65 eV and may also require adjustment when considering the initial plasma temperature.

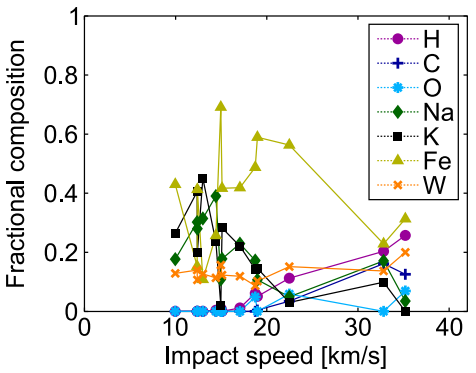

FIG. 12. Fractional composition of impact plasma from tungsten impacts as a function of impact speed.

C. Summary of results

Three major results were produced through this work. First, the initial temperature of the impact plasma is at least an order of magnitude lower than previously reported. A colder plasma will expand slower and will also shield itself against electric fields to a lower density because of its shorter Debye length. Thus, it will persist longer in a dense, non-collisional state, allowing for more RF emission.

Second, the composition of impact plasmas from glass targets has a low dependence on impact speed. This is indicative of a different ionization mechanism from tungsten. The SiO_2 covalent bonds present in the glass targets could produce ions through molecular dissociation, which is not a viable mechanism in metallic targets. Impacts at debris speeds may therefore pose a more significant threat on glass than on metal.

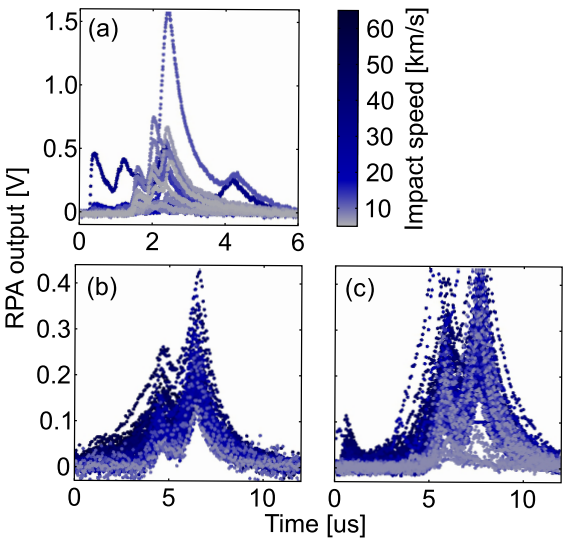

FIG. 13. Overlaid RPA measurements of impact plasma composition as a function of impact speed for (a) +1000 V tungsten, (b) +100 V uncoated solar cell, and (c) +100 V conductive OSR, color-coded for impact speed.

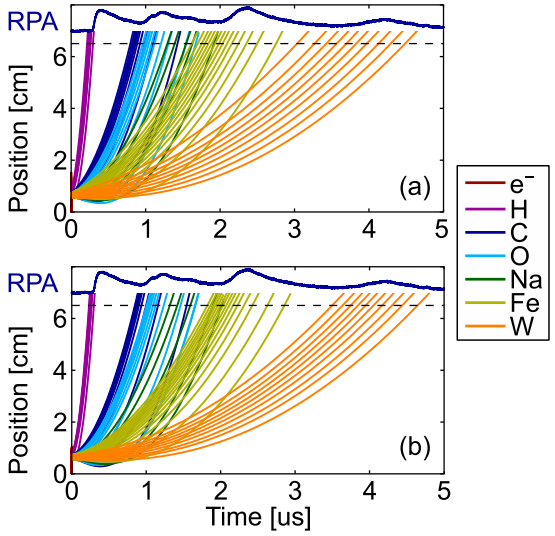

FIG. 14. (a) Simulation with composition and temperature computed by SPM model. (b) Same composition with temperatures reduced by factor of 10.

Finally, negative ion formation has a strong dependence on target material. In certain configurations, it is possible that the formation of negative ions results from the capture of free electrons, which indicates that the presence of negative ions will reduce the strength of a current pulse associated with the charge motion of the escaping electrons. A smaller population of accelerated electrons would produce weaker RF emission.

VI. CONCLUSIONS

The work presented here links plasma measurements to parameters much earlier in its expansion, enabling characterization of the plasma dynamics from when electron oscillation can occur up to when the plasma hits the sensor. Results of this study include the first measurement of impact plasma temperature considering internal electrostatic forces and of plasma composition from impacts on spacecraft materials.

These results can inform the spacecraft community with possible techniques to reduce the risk associated with hypervelocity impacts. Depending on the particular sensitivity of a spacecraft's electrical systems, impacts on negatively charged surfaces can be minimized to reduce the effect of electron current pulses, or impacts on neutral surfaces can be minimized to avoid RF emission from electron oscillation. The operation of existing satellites can be adjusted to account for the risk due to impacts on surfaces of different charge states. On future spacecraft, payloads and subsystems can be positioned and surface materials optimized to reduce the risk of effects from hypervelocity impact.

Characterizing the risk of electrical damage to spacecraft from hypervelocity impact is one step that will allow for safer and more robust utilization and exploration of space. Ultimately, we must develop a holistic understanding of all the hazards presented by the space environment in order to design a weatherproof spacecraft of the future—one that can detect external environmental threats and protect and repair its vulnerable systems.

ACKNOWLEDGMENTS

This study was sponsored by Los Alamos National Laboratory. The authors thank P. Colestock, S. Green, and the personnel of the Cosmic Dust Group at MPIK for their support during the experiments, J. Likar for the contribution of sample spacecraft materials, and J. Doolittle and G. King for their assistance in our plasma sensor calibration.

[1]R. D. Caswell, N. McBride, and A. Taylor, Int. J. Impact Eng. **17**, 139 (1995).
[2]N. McBride and J. A. M. McDonnell, Planetary Space Sci. **47**, 1005 (1999).
[3]H. Dietzel, G. Neukum, and P. Rauser, J. Geophys. Res. **77**, 1375, doi:10.1029/JB077i008p01375 (1972).
[4]P. R. Ratcliff, M. J. Burchell, M. J. Cole, T. W. Murphy, and F. Allahdadi, Int. J. Impact Eng. **20**, 663 (1997).
[5]L. Foschini, Europhys. Lett. (EPL) **43**, 226 (1998).
[6]R. Bianchi, F. Capaccioni, P. Cerroni, M. Coradini, E. Flamini, P. Hurren, G. Martelli, and P. N. Smith, Nature (London) **308**, 830 (1984).
[7]B. Jean and T. L. Rollins, AIAA J. **8**, 1742 (1970).
[8]M. J. Starks, D. L. Cooke, B. K. Dichter, L. C. Chhabildas, W. D. Reinhart, and T. F. Thornhill III, Int. J. Impact Eng. **33**, 781 (2006).
[9]K. Maki, T. Takano, A. Fujiwara, and A. Yamori, Adv. Space Res. **34**, 1085 (2004).
[10]E. C. Whipple, Rep. Prog. Phys. **44**, 1197 (1981).
[11]F. J. F. Osborne and M. A. Kasha, Can. J. Phys. **45**, 263 (1967).
[12]F. Melandsø and J. Goree, Phys. Rev. E **52**, 5312 (1995).
[13]A. Czechowski and I. Mann, Astrophys. J. **714**, 89 (2010).
[14]E. Grün, B. Gustafson, I. Mann, M. Baguhl, G. Morfill, P. Staubach, A. Taylor, and H. A. Zook, Astron. Astrophys. **286**, 915 (1994).
[15]Z. Ceplecha, J. Borovička, W. G. Elford, D. O. ReVelle, R. L. Hawkes, V. Í. Porubčan, and M. Šimek, Space Sci. Rev. **84**, 327 (1998).
[16]S. Close, P. Brown, M. Campbell-Brown, M. Oppenheim, and P. Colestock, Icarus **186**, 547 (2007).
[17]P. Brown, R. E. Spalding, D. O. ReVelle, E. Tagliaferri, and S. P. Worden, Nature (London) **420**, 294 (2002).
[18]D. Janches, S. Close, and J. T. Fentzke, Icarus **193**, 105 (2008).
[19]D. J. Kessler and B. G. Cour-Palais, J. Geophys. Res. **83**, 2637, doi:10.1029/JA083iA06p02637 (1978).
[20]S. Drapatz and K. W. Michel, Z. Naturforsch. A **29**, 870 (1974).
[21]K. Hornung, Y. G. Malama, and K. S. Kestenboim, Astrophys. Space Sci. **274**, 355 (2000).
[22]S. Close, P. Colestock, L. Cox, M. Kelley, and N. Lee, J. Geophys. Res. **115**, A12328, doi:10.1029/2010JA015921 (2010).
[23]A. Mocker, S. Bugiel, S. Auer, G. Baust, K. Drake, K. Fiege, E. Grün, F. Heckmann, S. Helfert, J. K. Hillier, S. Kempf, G. Matt, K. Otto, F. Postberg, H.-P. Röser, Z. Sternovsky, and R. Srama, Rev. Sci. Instrum. **82**, 095111 (2011).
[24]R. A. Heelis and W. B. Hanson, *Measurement Techniques Space Plasmas: Particles*, Geophysical Monograph 102 (American Geophysical Union, 1998), p. 61.
[25]A. J. Dekker, "Advances in research and applications," in *Solid State Physics*, edited by F. Seitz and D. Turnbull (Academic, 1958), Vol. 6, pp. 251–311.